Engineering Fracture Mechanics 307 (2024) 110282

Contents lists available at ScienceDirect

Engineering Fracture Mechanics

journal homepage: www.elsevier.com/locate/engfracmech

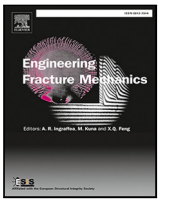

Statistical analysis of microstructurally small fatigue crack growth in three-dimensional polycrystals based on high-fidelity numerical simulations

Vignesh Babu Rao, Brian R. Phung, Bjorn T. Johnsson, Ashley D. Spear *

Department of Mechanical Engineering, University of Utah, Salt Lake City, 84112, UT, USA

ARTICLE INFO

Keywords:
CPFEM
FIP
Texture
Tilt and twist
Correlation analysis

ABSTRACT

Microstructurally small cracks (MSCs) are sensitive to their local microstructural neighborhoods, resulting in highly variable 3D crack propagation within individual samples and among a population of samples. Statistically quantifying this complex spatiotemporal variability requires collecting and analyzing a large number of 3D MSC growth observations, which remains challenging due to experimental constraints that limit the availability of 3D observations of MSCs in the existing literature. We address this gap by leveraging virtual observations of MSC growth using a state-of-the-art, high-fidelity simulation framework to provide a statistical perspective on 3D MSC growth behavior. The MSC growth simulations were performed in 40 unique but statistically similar polycrystalline microstructures, and the data extracted from the virtual observations were collectively analyzed to quantify variability in geometric, microstructural, and micromechanical aspects of MSCs. Variability in tortuosity, crack surface crystallography, and MSC growth parameters (local crack extension and kink angle) were quantified statistically. The results show that 3D MSC surfaces do not necessarily propagate along {111} crystallographic planes despite crack traces on radial planes being closely aligned with {111} slip plane traces. Also, the 3D MSC surfaces exhibit increasingly tortuous propagation and spatially varying local crack growth rates (with variability as high as 59% among the population). Moreover, a correlation study revealed some of the highly influential microstructural and micromechanical features controlling MSC growth parameters. The quantified variability holds direct implications for advanced materials prognosis in engineering applications, and the identified features from the correlation study can be leveraged to train machine learning models for rapidly predicting MSC growth behavior in the future.

1. Introduction

To date, the industrial design of most aerospace and mission-critical components is primarily based on the analysis of long cracks, which adhere to the concept of similitude. Their behavior is effectively characterized by the Paris law, which establishes a unique relationship between growth rate and stress intensity factor range within a specific material system. However, as we delve into the microstructurally small crack (MSC) regime — typically defined as cracks smaller than 10 times the grain diameter in a polycrystal [1] — the notion of a unique relationship between growth rate and stress intensity factor range starts to break down [1,2]. This shift is primarily due to the influence of local microstructural neighborhoods on MSCs, which results in a high

* Corresponding author.
E-mail address: ashley.spear@utah.edu (A.D. Spear).

https://doi.org/10.1016/j.engfracmech.2024.110282
Received 16 May 2024; Received in revised form 13 June 2024; Accepted 3 July 2024
Available online 15 July 2024

Nomenclature

Symbols

i	microstructural instantiation
j	crack front node
k	crack growth step
θ	angular position of vector connecting o and j with respect to Y-axis
$\vec{r}$	radial vector
d	equivalent grain diameter
a	half-crack length
Δa_j	crack extension at node j
Φ_j^{crit}	kink angle at node j
ΔCTD_j	crack tip displacement range at node j
ρ	Pearson correlation coefficient
d_{fs}^x, d_{fs}^y	nearest distance to the free surface in X and Y directions
E_{eff}	elastic modulus along the loading direction [001]
m	Schmid factor
ω	disorientation angle
TI	texture index
$\lambda_1, \lambda_2, \lambda_3, \lambda_4$	angle formed by the trace of the slip planes 1 to 4 on the radial plane with $\vec{r}$
λ_{clos}	closest of $\lambda_1, \lambda_2, \lambda_3, \lambda_4$ to Φ_j^{crit}
λ_m	one of $\lambda_1, \lambda_2, \lambda_3, \lambda_4$ that has the maximum Schmid factor
M_{micro}	micromechanical Taylor factor
D_5	fatigue indicator parameter
σ_{triax}	stress-triaxiality
$\sigma_1, \sigma_2, \sigma_3$	principal stresses
$\sigma_{xx}, \sigma_{yy}, \sigma_{zz}$	normal stresses
$\tau_{xy}, \tau_{yz}, \tau_{xz}$	shear stresses
$\epsilon_1, \epsilon_2, \epsilon_3$	principal strains
$\epsilon_{xx}, \epsilon_{yy}, \epsilon_{zz}$	normal strains
$\gamma_{xy}, \gamma_{yz}, \gamma_{xz}$	shear strains
$\Phi_{max(f)}$	angle along the probe path at which a feature f is maximum
$\Phi_{min(f)}$	angle along the probe path at which a feature f is minimum
$\Phi_{max(\nabla f)}$	angle along the probe path at which the spatial gradient of a feature f is maximum
Ω, Ψ	tilt and twist angles, respectively

degree of variability in their growth behavior. For instance, two MSCs with identical geometric and loading conditions may exhibit significantly different growth rates and propagation paths depending on their microstructural surroundings, thus violating the concept of similitude. For high-cycle fatigue scenarios, a majority of a fatigue crack's lifetime (upwards of 90%) is spent in the MSC regime [3,4]. Therefore, capturing the variability in MSC growth could potentially mitigate uncertainty in the residual life estimation and alleviate the need for overly conservative safety factors in the design phase of engineering components. Furthermore, the ability to predict fatigue crack growth in the MSC regime presents opportunities for early detection of potential structural issues and proactive maintenance.

Despite the potential benefits described above, a high degree of variability exhibited by MSCs — both within individual samples and among a population of samples — poses a significant challenge for capturing the variability and predicting their growth behavior. Extensive efforts have been undertaken in the literature to investigate the influence of various microstructural features on controlling MSC growth behavior and to develop empirical models for predicting crack behavior. Pioneering work on fatigue crack formation by Neumann [5,6] suggests that the early crack propagation occurs predominantly on the crystallographic glide planes (also known as stage-I cracking), thereby emphasizing the importance of the local grain orientation containing a propagating crack. Kunkler et al. [7] developed a mechanism-based numerical model based on experimental evidence in which fatigue cracks initially grow along a single slip plane. As additional slip systems become active, cracks tend to propagate along alternating slip bands, eventually manifesting in mode I growth. Zhai et al. [8] showed with experimental evidence that the tilt and twist angles between a crack (propagating along a slip plane) and the next favored slip plane across a grain boundary are the key parameters controlling the path and growth rate of a short crack. They associated higher twist angles with crack retardation at the grain boundaries. The

Schmid factor of the slip planes and the geometric compatibility factor have also been shown to play a role in governing MSC propagation.

However, while experimental analyses offer qualitative insights into the influence of various microstructural features on MSC growth, their applicability is strictly limited to the analyzed samples. Thus, relying solely on experiments is insufficient to predict the variable nature of MSCs. Therefore, microstructure-sensitive computational modeling has emerged as a valuable supplement to studies involving MSC growth behavior. Numerical simulations using calibrated crystal plasticity models enable access to the micromechanical fields ahead of the crack front, which are challenging to obtain via experiments. These micromechanical fields are then correlated to the growth behavior through a suitable fatigue indicator parameter (FIP). McDowell et al. [9] employed 2D crystal plasticity simulations of experimentally measured microstructure and proposed plastic strain accumulation could be used as a FIP, as they found the growth of MSCs is associated with the regions of highest plastic strain accumulation. Rovinelli et al. [10,11] used crystal plasticity simulation to complement experimental observations and tested the predictability of various slip-based small crack driving force metrics. Proudhon et al. [12] simulated 3D short crack propagation in an experimentally observed microstructure based on a FIP similar to one proposed by Hochhalter et al. [13] and reported short crack features such as deviation of crack at the grain boundary and effect of the twist angle on the crack retardation are in good agreement with experimental findings.

Although there are experimental and numerical studies focused on understanding the underlying causes of variability in MSC growth, so far, little to no effort has been made to quantify the extent of this variability in a statistical sense in any material system despite the potential industrial significance of doing so. This gap exists because statistically quantifying such variability would require collecting a substantial number of 3D observations of MSC growth within the same material system, either through experiments or simulations, to achieve statistical significance – a task that is exceedingly challenging using the current state-of-the-art systems. On one hand, collecting 3D observations of MSC growth via experiments is constrained by the time, cost, and sophisticated equipment requirements, particularly given the microstructural length scale of MSCs. On the other hand, high-fidelity numerical simulations suffer from being computationally heavy. Nonetheless, addressing these challenges is crucial for capturing the inherent variability of MSCs within any material systems, as well as elucidating important couplings that could exist between the microstructure and MSC growth behavior.

The objective of this work is to conduct statistical analysis on data extracted from a large number of virtual 3D observations of MSC growth. The virtual observations are generated using a high-fidelity numerical simulation framework that relies on a state-of-the-art remeshing approach along with a crystal plasticity constitutive model to accurately predict the micromechanical fields near an explicitly resolved crack front. MSCs that are assumed to have an initial semicircular shape are propagated in 40 microstructural instantiations using the high-fidelity simulation framework. Data collected along discrete crack fronts from 40 simulations yield 7400 data points that are used to quantify the variability in MSC growth parameters, namely local crack extension and kink angle. The crystallography of the evolved crack surfaces is studied to characterize the texture preference of MSCs. Finally, a correlation analysis is conducted to determine the relative importance of various microstructural and micromechanical features in predicting the MSC growth parameters.

2. Methods

2.1. High-fidelity simulation

In the absence of sufficient experimental observations, we elect to conduct many virtual observations of 3D MSC propagation in polycrystalline microstructures using a high-fidelity simulation workflow. The workflow comprises an in-house voxel-based remeshing framework [14], an in-house tool called Crackmesher [15], DREAM.3D [16], and a commercial finite-element solver with a crystal plasticity constitutive model. The entire crack-simulation workflow is detailed in the following subsections.

2.1.1. Synthetic microstructure generation

Each crack-growth simulation starts by generating a synthetic voxel-based representation (VBR) of a polycrystalline microstructure using DREAM.3D [16]. The microstructure contains $150 \times 75 \times 100$ voxels representing a physical volume of $150 \times 75 \times 100$ μm with a resolution of 1 μm per voxel edge. The microstructural volume is packed with equiaxed grains comprising random crystallographic orientations and is intended to represent Al–Mg–Si alloy [17]. The grain size follows a log-normal distribution having a mean equivalent spherical diameter of 27 μm and a standard deviation of 4 μm. There are approximately 120 grains in each microstructure. One of the generated microstructures along with the orientation distribution function (ODF) used to generate random crystallographic orientations (no texture) is shown in Fig. 1a. In total, 40 microstructural instantiations were created. While the microstructural instantiations are statistically similar, each is unique in terms of its precise microstructural arrangement of grains and crystal orientations. All 40 microstructural instantiations are presented in the Appendix A.

2.1.2. Explicit crack insertion and adaptive remeshing

The voxel-based remeshing framework developed by Phung and Spear [14] forms the foundation for the crack simulation framework by performing crucial tasks such as crack insertion and conformal meshing. The VBR of the microstructure and a point cloud of the crack geometry serve as inputs to the framework. For more details, the reader is referred to Ref. [14]. In this work, a semicircular surface crack of length $2a = 48$ μm is inserted into the VBR of the microstructure in a mode I orientation, as shown in Fig. 1b. The voxel-based remeshing framework partitions the grains in the VBR based on the user-provided crack geometry. All grains, both partitioned and unpartitioned, are then surface meshed individually using DREAM.3D [16], which results in a uniform

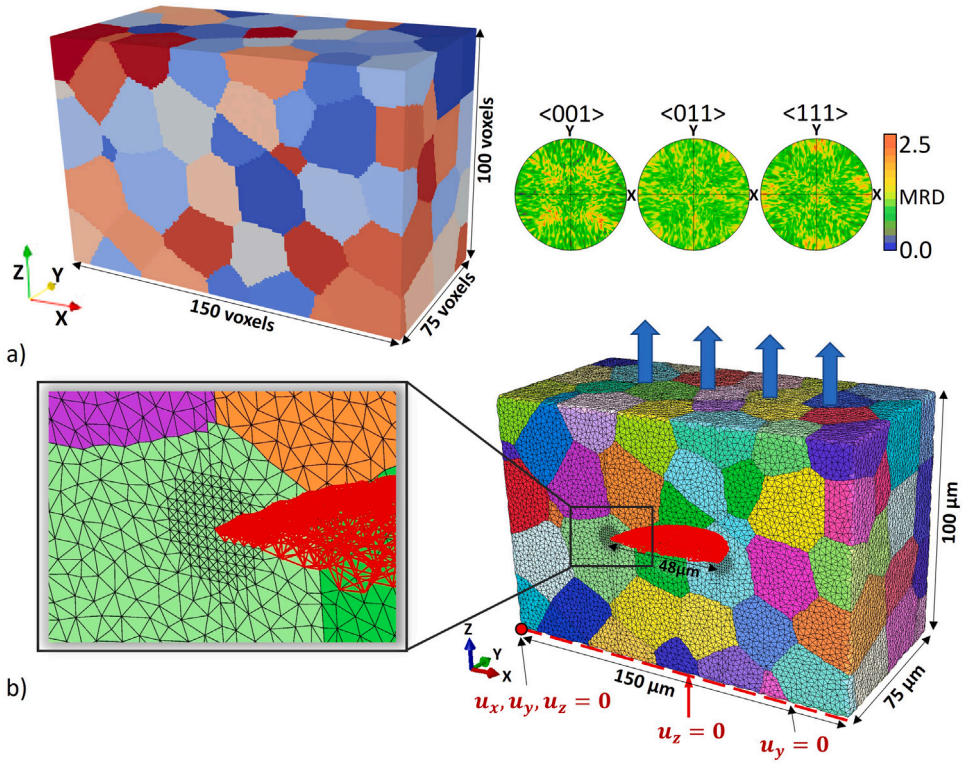

Fig. 1. (a) One of 40 synthetic microstructures prior to crack insertion and the corresponding ODF showing the random distribution of crystal orientations. (b) Meshed microstructure with an initial semicircular surface crack inserted using a voxel-based remeshing framework and with boundary conditions depicted. A portion of the mesh is magnified to illustrate the local mesh refinement applied near the crack front and mesh coarsening applied to the far field.

mesh that is conformal to the grain boundaries and crack surface. A Laplacian smoothing is applied to alleviate the stair-step effect of the VBR. The initial uniform mesh is used as an input to an in-house surface mesh gradation tool [15] that allows selective control of the element size distribution via edge-splitting and edge-collapsing algorithms. Using this tool, elements close to the crack-front (near-field mesh) are refined, and elements far from the crack-front (far-field mesh) are coarsened to achieve target element edge lengths of 0.8 μm near the crack front and 2.5 μm away from the crack front, respectively. The gradated surface mesh is then converted into a suitable volume mesh consisting of linear tetrahedral elements. The target values for the element size were determined by a mesh convergence study performed to verify the convergence of MSC growth parameters, namely the crack extension and kink angle. In this study, the far-field element size is fixed, and the near-field element size is progressively reduced until the MSC growth parameters converge within a 5% error tolerance. This type of mesh gradation allows for the convergence of MSC growth parameters with fewer total number of elements compared to a uniform mesh, providing a significant computational advantage during the simulation as documented in Ref. [15].

2.1.3. Boundary and loading conditions

Once the mesh is generated, the boundary conditions are applied to simulate fatigue loading conditions. Nodal displacements on the bottom face are constrained in the Z-direction. In order to prevent rigid body rotation, all degrees of freedom were arrested for the node at the origin, and the nodes along the bottom front edge were constrained in the Y-direction, as shown in Fig. 1b. This type of boundary condition containing four free surfaces is similar to the "minimal" boundary condition examined by Stopka et al. [18], which provided faster convergence of FIP metrics while being least restrictive among other non-periodic boundary conditions investigated in their study. Vertical displacement is applied on the top surface via strain control with a maximum applied strain of 0.2% and a loading ratio $R = 0.1$ to simulate one complete cycle of fatigue loading (loading, unloading). The decision to simulate one fatigue cycle is based on a kink angle convergence study. In this study, three fatigue cycles were simulated in a microstructural instantiation with an initial crack, and the kink angle along the crack front was evaluated (as described in Section 2.1.5) at the maximum applied strain of each of the three fatigue cycles. The variation in kink angle among those calculated from three fatigue cycles was less than 1%.

2.1.4. Crystal plasticity constitutive model

The finite element implementation of an elasto-viscoplastic constitutive model is used to define material behavior. The constitutive model is based on crystal plasticity theory and is implemented as a user element subroutine in ABAQUS®. For more

Table 1
Calibrated crystal-plasticity parameters and Lamé constants [20].

$\dot{\gamma}_0$ (s^{-1})	m	G_0 (MPa)	g_0 (MPa)	λ (MPa)	μ (MPa)
0.05	0.0049	150.0	95.5	50 775.0	24 800.0

details regarding the implementation, the reader is referred to Matouš and Maniatty [19]; however, some key aspects of the crystal plasticity model are briefly discussed here.

When materials deform, the deformation gradient tensor, $\boldsymbol{F}$, acts as a linear transformation between the reference configuration and the current configuration:

$$\mathrm{d}\boldsymbol{x} = \boldsymbol{F}\mathrm{d}\boldsymbol{X} \ , \tag{1}$$

where $\boldsymbol{X}$ and $\boldsymbol{x}$ denote the position vector of any arbitrary point in reference and current configurations respectively. The deformation gradient tensor, $\boldsymbol{F}$, is multiplicatively decomposed into an elastic component, $\boldsymbol{F}^{\mathrm{e}}$, that accounts for the elastic stretching and rigid body rotations and an isochoric plastic component, $\boldsymbol{F}^{\mathrm{p}}$, as follows:

$$\boldsymbol{F} = \boldsymbol{F}^{\mathrm{e}}\boldsymbol{F}^{\mathrm{p}}. \tag{2}$$

The plastic velocity gradient, $\boldsymbol{L}^{\mathrm{p}}$, expressed in terms of the plastic deformation gradient, is related to the superposition of crystallographic slip rate, $\dot{\gamma}^{\alpha}$, on n_s slip systems:

$$\boldsymbol{L}^{\mathrm{p}} = \dot{\boldsymbol{F}}^{\mathrm{p}}\boldsymbol{F}^{\mathrm{p}-1} = \sum_{\alpha=1}^{n_s} \dot{\gamma}^{\alpha}\boldsymbol{P}^{\alpha}. \tag{3}$$

The idea of accommodating plastic deformation by shear deformations along each slip system is foundational to the crystal plasticity theory. In this work, as we model a face centered cubic (FCC) material system, the slip evolution along 12 octahedral slip systems, i.e., slip on four {111} planes in three ⟨110⟩ directions, is considered. The term $\boldsymbol{P}^{\alpha}$ denotes the Schmid tensor, which is a dyadic product of the slip direction, $\boldsymbol{s}^{\alpha}$, and the slip plane normal, $\boldsymbol{m}^{\alpha}$, for the slip system α:

$$\boldsymbol{P}^{\alpha} = \boldsymbol{s}^{\alpha} \otimes \boldsymbol{m}^{\alpha}. \tag{4}$$

The slip rate on a slip system is defined by a power law flow rule that describes the dependence of slip rate on individual slip systems as a function of resolved shear stress, τ, and slip resistance, g, as follows:

$$\dot{\gamma}^{\alpha} = \dot{\gamma}_0 \frac{\tau^{\alpha}}{g^{\alpha}} \left| \frac{\tau^{\alpha}}{g^{\alpha}} \right|^{\frac{1}{m}-1}. \tag{5}$$

The term $\dot{\gamma}_0$ indicates a reference slip rate, and m denotes a rate-sensitivity parameter. The slip resistance, g^{α}, evolves based on a Voce–Kocks type hardening rule, where all 12 slip systems harden at the same rate. The calibrated parameters for the crystal plasticity model are similar to those reported in Ref. [20]. For the list of crystal plasticity parameters and their calibrated values, refer to Table 1.

2.1.5. Crack growth rules and MSC growth

The meshed polycrystalline geometry with an explicit geometric discontinuity representing the crack surface is analyzed using ABAQUS® standard solver to compute local stress and strain fields ahead of the 3D crack front. Crack growth parameters (viz., Δa and Φ^{crit}) are evaluated at each node j along the crack front according to the following rules.

The local crack growth rate is modeled as a function of the cyclic crack tip displacement range (ΔCTD) [21,22]:

$$\frac{\mathrm{d}a}{\mathrm{d}N} = G(\Delta CTD - \Delta CTD_{th}) \ , \tag{6}$$

where G is a proportionality constant that represents the mechanical irreversibility of slip near the crack tip due to cyclic loading and is taken as 0.1 [22], and ΔCTD_{th} is the threshold value for a non-propagating crack and is taken as 5×10^{-10} m [22]. We elect to use ΔCTD because it has been shown to serve as a surrogate for the crack driving force in MSCs [7,21,23]. From the local crack growth rate, we estimate Δa, by assuming ΔN to be a constant (1500 cycles) as follows:

$$\Delta a = G(\Delta CTD - \Delta CTD_{th})\Delta N \ . \tag{7}$$

The cyclic crack tip displacement range at a given node j, i.e., ΔCTD_j, is calculated between the maximum and minimum points along the unloading portion of the applied cyclic displacement and is measured by finding the euclidean distance between the surfaces of the crack 1 μm behind the crack front node (consistent with experimental measurements [24]). This is illustrated in Fig. 2, where the position of a radial plane relative to a crack front node, j, along the crack front is shown in Fig. 2a, while the measurement of CTD behind the node j, on that radial plane is depicted in Fig. 2b.

The direction of crack propagation, or the kink angle (Φ_j^{crit}), is estimated at each crack front node j using a modified Fatemi–Socie metric designated as D_5 by Hochhalter et al. [13]:

$$D_5 = \max_p \int_0^t \sum_{\alpha=0}^{N_d} \left| \dot{\gamma}_p^{\alpha} \right| \left(1 + k \frac{\langle \sigma_n^p \rangle}{g_0} \right) \mathrm{d}t \ , \tag{8}$$

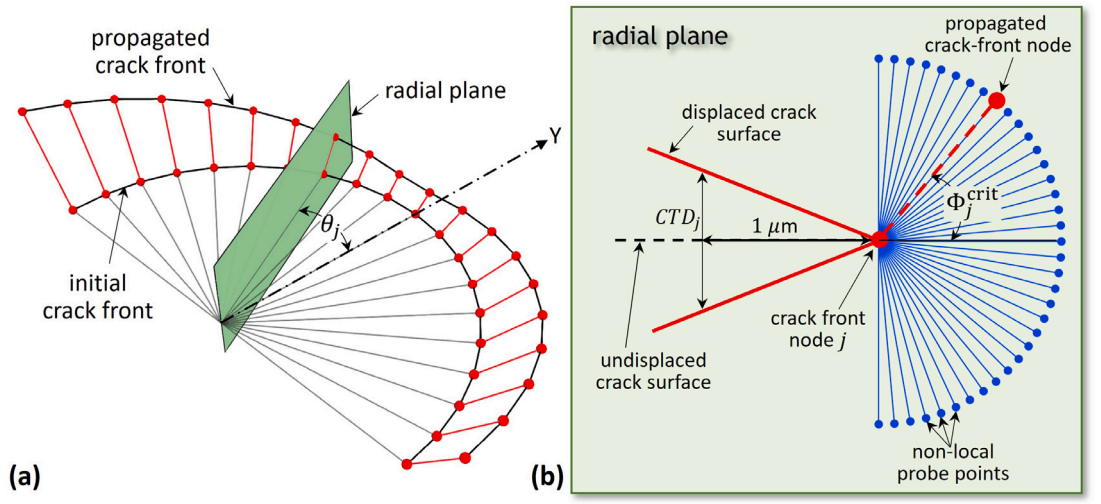

Fig. 2. Schematic diagram showing the measurement of CTD behind the crack front node and the estimation of kink angle using non-local probe points ahead of the crack front node.

where $\langle \sigma_n^p \rangle$ is the normal tensile stress acting on slip plane p, g_0 is the initial hardness of the slip system, k is a parameter that dictates the importance of tensile stress relative to plastic slip, and N_d is the number of slip directions on a given slip plane.

The D_5 metric is evaluated at 181 points along a semicircular non-local probe path of radius 4.8 μm[1] centered around crack-front node j, as shown in Fig. 2b. Typically, the D_5 metric along the non-local probe shows a distinct primary peak with maximum D_5 accumulation, often accompanied by one or two secondary peaks with less D_5 accumulation depending on the orientation of slip planes and their degree of activation. The direction along the probe, Φ (with respect to the X-axis), where the D_5 metric has a maximum value (i.e., the primary peak), is interpreted/postulated as Φ^{crit} at j as follows:

$$\Phi_j^{crit} = \underset{\Phi}{\text{argmax}}(D_5) \ . \tag{9}$$

However, calculating Φ^{crit} along the crack front at discrete nodes leads to spurious spikes that are neither physically meaningful nor easy to simulate. An example is shown in Fig. 3, where the raw angular probe-path positions corresponding to primary and secondary D_5 peaks are plotted for distinct crack front nodes along the crack front. Spikes associated with the curve by simply connecting the primary peaks can be seen in Fig. 3. The spikes stem from numerical instabilities and are alleviated by applying a grain-level conditioning scheme. To apply grain-level conditioning, the crack front is first partitioned into sub-regions based on the intersection of grain boundaries (dashed vertical lines in Fig. 3) with the crack front. Nodes causing spurious spikes within each sub-region (if any) are identified, and Φ^{crit} for those nodes are reassigned to the direction of a secondary peak that is closer to other primary peaks of the neighboring non-spurious nodes within the sub-region. The motivation for this grain-level conditioning is that it is physically unlikely for a crack front to bifurcate abruptly within the same grain.

Once Δa_j and Φ_j^{crit} at each node j are determined, the point cloud containing the crack surface is updated. The updated crack surface is inserted back into the VBR of the microstructure, and the entire process of simulating the MSC growth is repeated to simulate further crack propagation. Five crack growth increments are simulated in each of the 40 microstructural instantiations, resulting in 200 increments of virtually observed crack propagation. Fig. 4 illustrates the incremental nature of MSC propagation in the high-fidelity simulation by showing the crack surface at each crack growth increment. Further, discretizing each crack front enables collection of massive data (n = 7400 crack front points) to assess crack growth variability and perform statistical correlation analysis.

2.2. Quantifying variability in MSC growth

Microstructure-sensitive growth characteristics of the MSCs are assessed by quantifying the variability in geometric, microstructural, and micromechanical aspects of MSCs. The variability in geometry is assessed based on a tortuosity metric. Microstructural variability is assessed by analyzing the crack surface crystallography. Micromechanical variability is assessed based on the MSC growth parameters, namely, Δa and Φ^{crit}.

[1] The radius of the non-local probe is taken as 20% of the initial half-crack length, a, which is within the bounds suggested in Ref. [13].

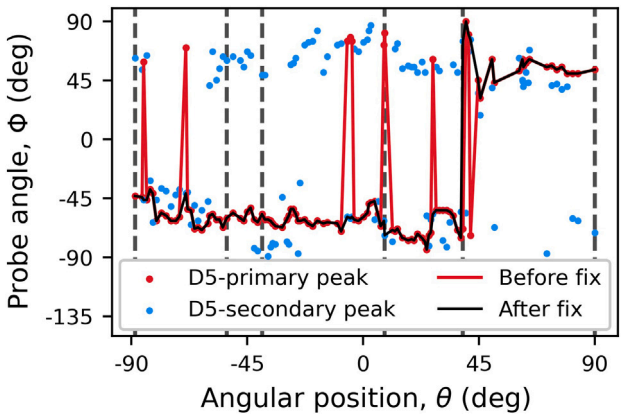

Fig. 3. Plot showing kink angles before and after applying a grain-level conditioning scheme to fix the spurious spikes observed while determining kink angle at discrete nodes along the crack front. Scatter points indicate the angle of primary and secondary D_5 peaks along the semicircular probe. Dashed lines indicate grain boundary intersections.

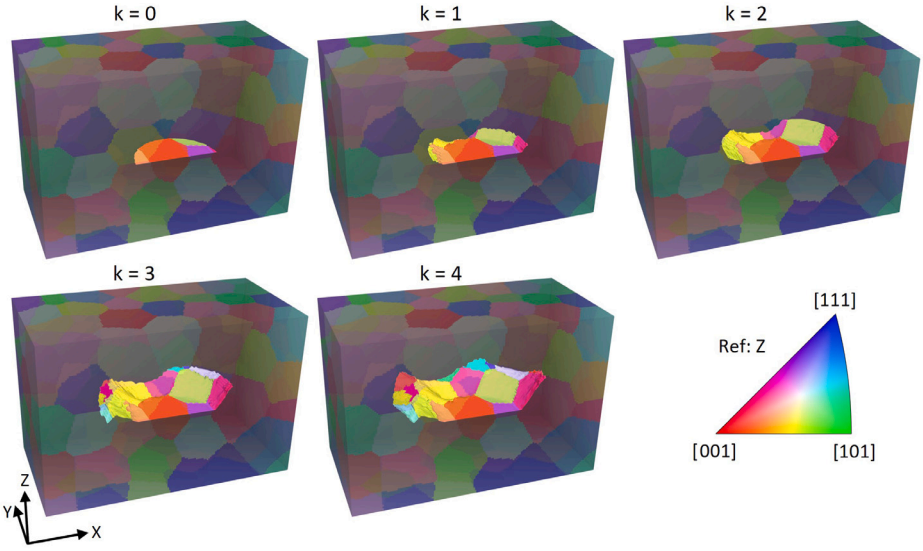

Fig. 4. Simulated incremental growth of a 3D MSC in a polycrystalline microstructure, where k in the figure corresponds to the crack growth increment. Grains are colored according to their crystal orientation using an inverse pole figure (IPF) map.

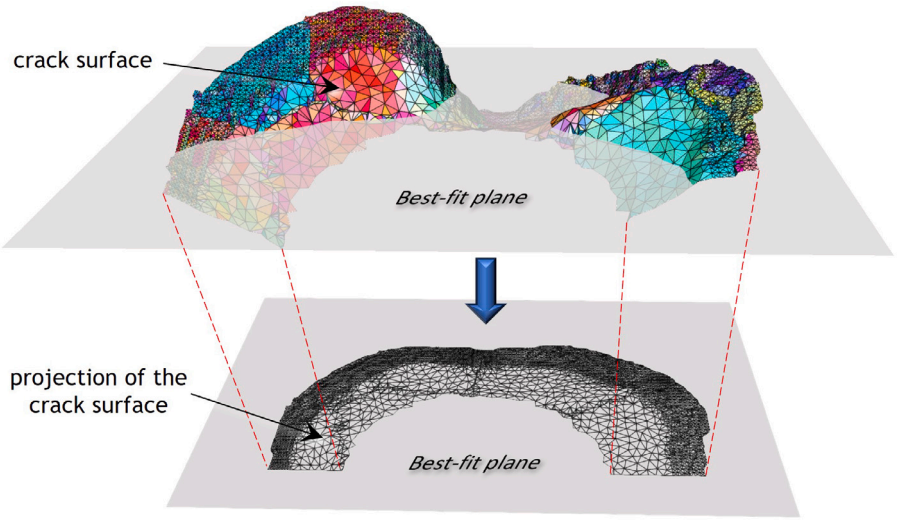

Fig. 5. Illustration of a tortuous crack surface (omitting the initial planar portion) along with its projection on the best-fit plane. The best-fit plane is shifted downwards to visualize the projection of the crack surface.

2.2.1. Tortuosity

We define tortuosity as the deviation of a surface from being planar. Mathematically, it is defined as the ratio of the true area of the tortuous surface, A_t, to its projected area on the best-fit plane, A_p:

$$\tau = \frac{A_t}{A_p}. \tag{10}$$

Fig. 5 shows a meshed, incremental crack surface whose true area is estimated by summing up the area of the triangular facets comprising the crack surface. These individual triangles are projected onto the best-fit plane, and the projected area is calculated. The best-fit plane is determined by performing weighted principal component analysis on the point cloud of the evolved crack surface. The eigenvector corresponding to the smallest eigenvalue represents the normal of the best-fit plane, as illustrated in Fig. 5.

2.2.2. Crystallographic texture of MSCs

To assess the evolution of crack-path crystallography with respect to crack propagation, we quantified the texture of the initial crack surface and compared it with the texture of the propagated crack surface. Fig. 6a shows a triangulated initial crack surface from one of the high-fidelity simulations, and Fig. 6b shows the same crack surface after four propagation steps (excluding the initial crack). The crack-surface crystallography is quantified by first calculating the surface normal for each of the triangulated facets in the global coordinate system. A coordinate transformation is then applied to represent the facet normals in the crystal coordinate system using the Euler angles of the grain with which each triangle is associated. To visualize the crystallographic planes along the crack surface, the normals are mapped to their respective inverse pole figure (IPF) colors, as shown in Fig. 6. A pole density function with due respect to the crystal symmetry (m-3m) is generated using the unit facet normals of all triangles represented in the crystal coordinate system and is plotted in an irreducible stereographic triangle, which will be discussed in Section 3.2. A Python module, orix [25], is used to generate pole density functions and plot inverse pole figures.[2]

2.3. Data collection for correlation analysis

Correlations between various features and the MSC growth parameters (Δa and Φ^{crit}) are quantified by the Pearson correlation coefficient, ρ, which measures the strength of the linear relationship between two quantitative variables. The extracted features are divided into three categories: geometric, microstructural, and micromechanical. The feature extraction and processing techniques employed to study the correlations with Δa differ from those used to study the correlations with Φ^{crit}. This difference is based on the rationale that, unlike Δa, Φ^{crit} is a direction-based metric and therefore requires direction-dependent features. The two different strategies used for correlation analysis are summarized as follows.

The feature-extraction strategy for the Δa correlation study involves placing 3D cubic sampling grids at crack front nodes along a given crack front, as illustrated in Fig. 7a. For visualization, only four grids are shown in the figure; however, sampling grids

[2] Because the discretized crack surface contains a non-uniform mesh size, appropriate weights have been assigned to each of the facet normals commensurate with their respective facet area while generating the pole density function.

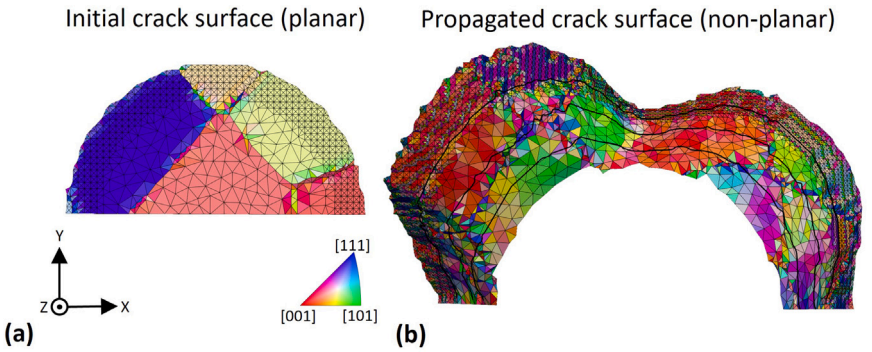

Fig. 6. Crack surface crystallography for one of 40 MSC growth simulations: (a) initial crack surface, and (b) final crack surface after four MSC propagation steps (excluding the initial crack) demarcated by black curves.

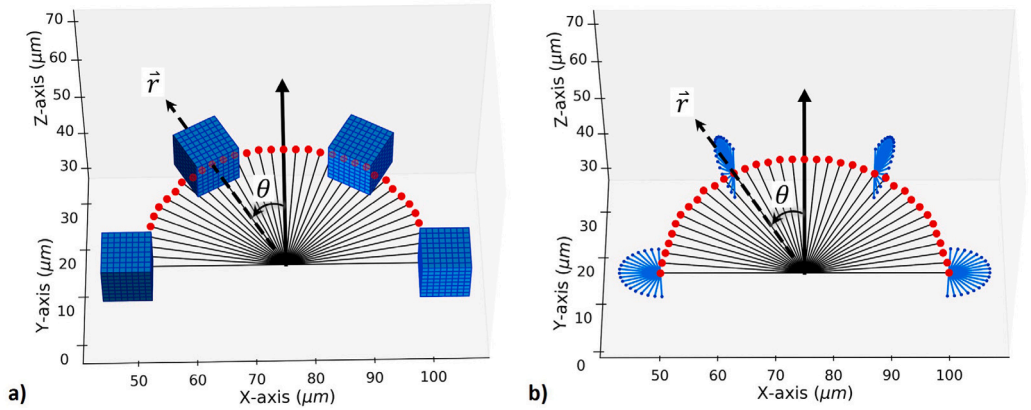

Fig. 7. Illustration of data-extraction processes to support correlation analysis: (a) 3D grids are placed at nodes along the crack front for analysis of Δa. (b) Semicircular probes are placed at nodes along the crack front for analysis of Φ^{crit}.

are placed at 5° intervals along the crack front, resulting in 37 grids for any given crack configuration. Each 3D grid has a local Cartesian coordinate system, denoted X', Y', Z', and is aligned such that the X'-axis of the grid is orthogonal to the radial vector and the Y'-axis of the grid is parallel to the radial vector. Each sampling grid is positioned along the radial direction such that more data points (about 80%) are sampled ahead of the crack front node than behind the crack front node. The grid size is determined by a grid-size study, where grid sizes with edge lengths ranging from 3 μm to 12 μm are investigated, and the one that produces maximum correlation between Δa and the D_5 metric is selected. Note that the purpose of this grid-size study is to ensure that the features are sampled from a relevant volume of material that captures localized micromechanical fields ahead of the crack while minimizing the inclusion of non-crack tip fields. A 3D grid with edge lengths of 8 μm is found to be optimal by this study, and this grid size is consistently applied to collect all input features. The resolution of the grid is set to 1 μm, which is approximately the element size near the crack front. Geometric, microstructural, and micromechanical features are extracted at grid points within each sampling grid. After extracting the features as 3D arrays, they are averaged, thereby reducing the 3D array to a single real-valued output for each sampling grid, which is then correlated with Δa at the corresponding position.

The feature-extraction strategy for the Φ^{crit} correlation study involves placing semicircular probes ahead of all crack front nodes, as illustrated in Fig. 7b. For visualization, only four probes are shown; however, the sampling probes are placed at 5° intervals along the crack front that results in 37 probes in any given crack configuration. The sampling probe is centered about the crack front node, and all points on the probe are contained within the radial plane. Geometric, microstructural, and micromechanical features are extracted at the probe points. After extracting the features along the semicircular probe, the direction, Φ, along the probe path at which a given feature value is maximized is designated as the direction-dependent descriptor of that feature.

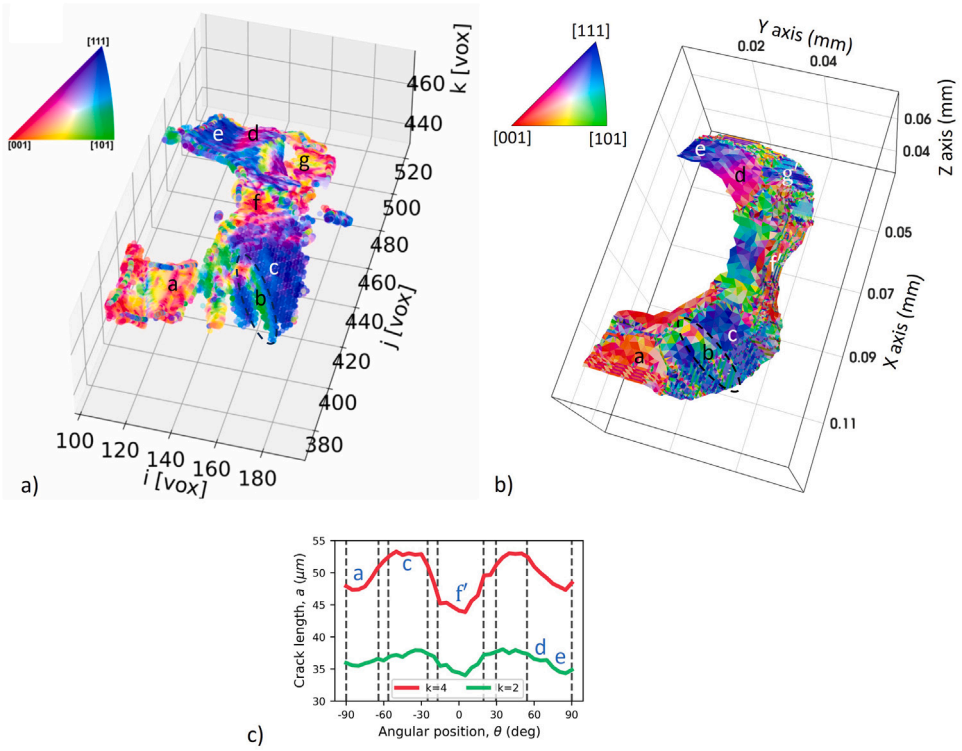

Fig. 8. IPF-colored local crack surface normals of (a) an experimentally propagated crack (initiated from a FIB notch) by Menasche et al. [26] and (b) a numerically simulated crack (initiated from an initial half-penny crack) using high-fidelity framework by present work. (c) Crack length as a function of the position along the crack front at two different growth increments, $k = 2$ and $k = 4$. The dashed vertical lines correspond to grain boundaries that intersect the crack front at the increment $k = 4$.

As this probing strategy is similar to the non-local probing technique used to estimate Φ^{crit} itself, we know as *a priori* that a similar probe radius should maximize the correlations of kink angle with the direction-dependent D_5 metric. Therefore, the radius of the probe is chosen as 4.8 μm and the angular resolution of the probe is set to 1°. It is noted, however, that the goal is to assess the correlations between Φ^{crit} and a variety of geometrical, microstructural, and micromechanical features, but we use correlations with D_5 as a verification parameter (i.e., we expect it to have the highest correlation)

3. Results and discussion

3.1. Comparison between simulated and experimentally observed crack surfaces

In this section, we compare qualitatively the characteristics of simulated MSCs from this work with those of experimental observations available in the literature to evaluate the effectiveness of the simulation framework for generating realistic MSC growth.

In Fig. 8, an experimentally observed 3D crack surface reported in a recent paper by Menasche et al. [26] is compared with a representative crack surface from the present work. Both Figs. 8a and 8b show the geometry of the propagated crack surfaces with colors representing the crack surface crystallography in the IPF convention. It is noted that the experimental fatigue crack is initiated from a FIB notch in a Ni-based superalloy specimen; whereas, the simulated crack is initiated from a half-penny crack in Al–Mg–Si alloy. Both microstructures have FCC crystal structures.

Visually, the regions marked as *a*, *c*, *d*, and *e* in Fig. 8a have approximately similar crystallography at similar locations in Fig. 8b. Interestingly, a band-like feature, marked as *b* in Fig. 8a, is also observed in Fig. 8b in close proximity to region *c*. Moreover, a similarity in crack morphology is also observed near *b* and *c*, where the crack takes a steep slope downward in both Figs. 8a and 8b (not very obvious because of the viewpoint).

One of the key findings from Ref. [26] was that the crack propagation was rapid along {111} planes, such as the regions indicated as *c* and *e* in Figs. 8a and 8b. The crack growth was relatively slower in regions *a* and *f*. To verify if the simulated crack exhibits this behavior, the crack length of the simulated crack is plotted as a function of angular location along the crack front in Fig. 8c at two different crack growth steps. The dashed vertical lines in Fig. 8c indicate the intersection of the crack front, $k = 4$, with the

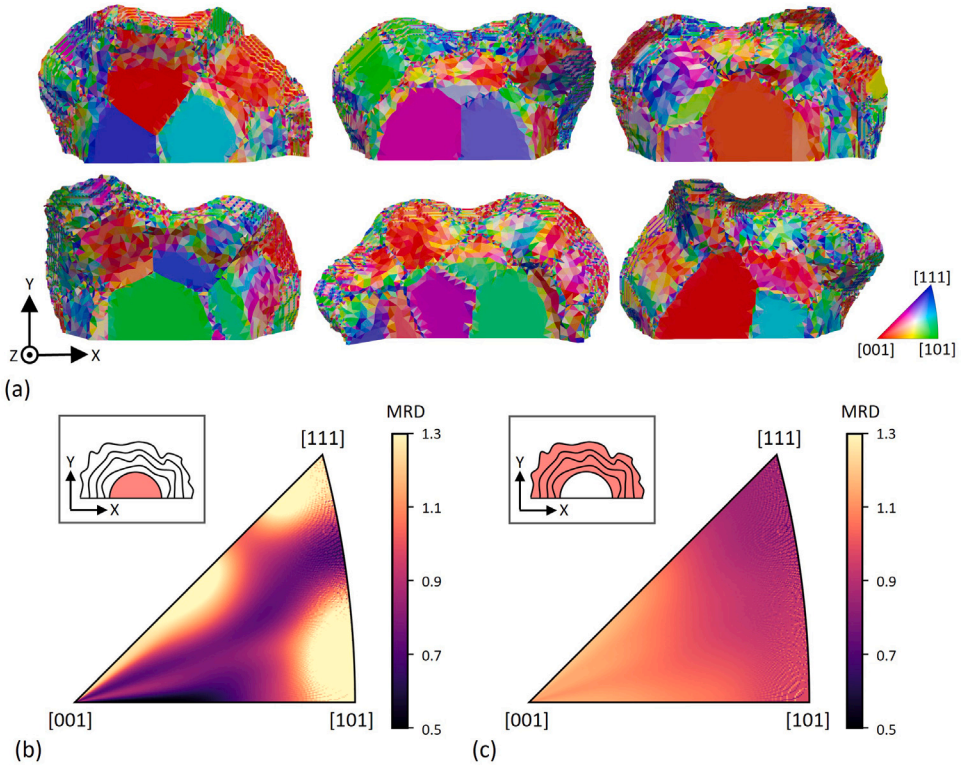

Fig. 9. (a) Crack-surface crystallography of simulated MSCs from six out of 40 instantiations. The IPF colors on the crack surfaces indicate the local crack-facet normals resolved in crystal reference frame. Crack-surface crystallography for all 40 MSC simulations represented as density plots on irreducible stereographic triangles: (b) initial crack surface and (c) propagated crack surface. Insets highlight the crack surface whose facet normals were used to generate the corresponding density plots.

grain boundaries. The regions corresponding to Fig. 8b are labeled approximately in Fig. 8c. It can be seen that the crack length corresponding to regions c, d, and e have relatively larger crack lengths compared to the regions a and f'. This implies that the crack growth rate near regions c, d, and e are higher relative to the regions a and f', which is consistent with their experimental findings.

Despite differences in material composition and crack initialization between the experimental and simulated crack, the striking similarities observed in the propagated crack, including crack morphology, crystallography, and rapid crack propagation regions, instill confidence in high-fidelity simulations in capturing the critical aspects of MSC propagation.

3.2. Crystallographic texture of virtually observed crack surfaces

This section compares the crack surface crystallography of initial crack surfaces with that of the propagated crack surfaces from the entire population of 40 instantiations to investigate if the tortuous crack surfaces exhibit crystallographic texture with respect to the initial flat cracks. Fig. 9a visualizes the propagated crack surfaces in six simulated instantiations (only for visual representation — the texture analysis is conducted with data from all 40 simulated crack surfaces). The colors on the crack surfaces indicate the local crack-facet normals resolved in crystal reference frame with the IPF convention. All 40 crack-surface crystallography maps are presented in Appendix A.

Fig. 9b shows the distribution of crack surface normals resolved in their local crystallographic coordinates for the initial cracks from all 40 instantiations. As shown in Fig. 9b, the initial crack does not exhibit significant crystallographic texture, which is expected given that the initial cracks were inserted arbitrarily without regard for crystal orientation (similar to FIB notches introduced in experiments). Fig. 9c shows the crystallography of the propagated crack surfaces from all 40 instantiations. The intensities shown in Fig. 9c indicate no texture on the propagated crack surface. The absence of higher intensity regions near {111} planes suggests that these cracks did not propagate along the {111} slip planes, contrary to what is generally observed in stage-I crack growth. We observed this behavior despite the fact that the direction of crack propagation in this work is modeled based on the D_5 metric, which accounts for slip occurring on {111} octahedral planes.

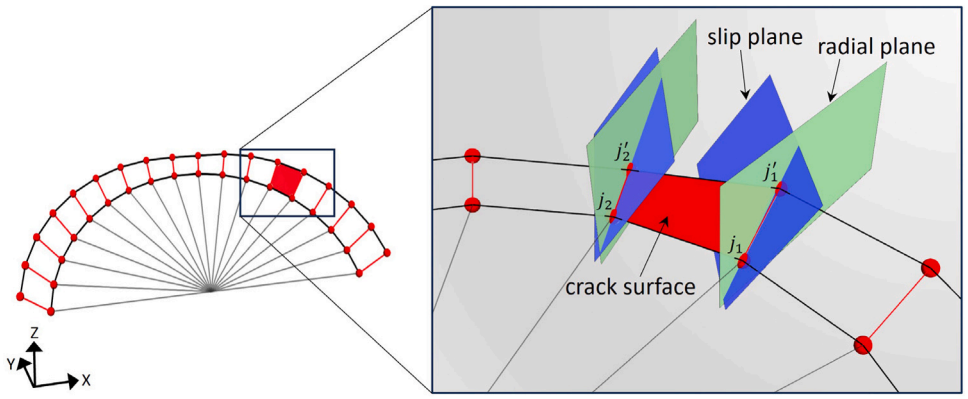

Fig. 10. Schematic illustration of the orientation of slip planes and radial planes with respect to the crack surface. Note that crack propagation aligns with the trace of the slip plane when viewed on the radial plane despite the 3D crack surface not coinciding with the slip plane.

To provide geometric reasoning behind the non-conformal crack propagation to the slip planes, Fig. 10 schematically depicts the orientation of slip planes (blue) and radial planes (green) at two neighboring crack front nodes, j_1 and j_2, contained within the same grain. The first thing to note from Fig. 10 is the alignment between the trace of the slip plane and the trace of the crack surface (e.g., j_1 to j_1') with respect to the radial planes. In other words, 2D observations of crack growth on the radial planes suggest crack propagation along the slip plane. However, in 3D, it can be seen that the crack surface (formed by j_1, j_2, j_2', and j_1') does not necessarily align with the slip plane. This occurs when the slip plane is twisted relative to the local crack surface. The crack surface coincided with a slip plane in 3D for cases where the twist angle is minimal. Examples can be seen in Fig. 8b, where portions of the crack that propagated along {111} slip planes (blue) had a minimal twist angle. These results imply that the direction of the crack kink, Φ_j^{crit} (based on the direction of D_5 localization), is mostly influenced by the tilt angle of the highly activated slip plane, while the twist angle has a minor effect.

Another less obvious reason for the lack of texture is an artifact of the implementation used for crack extension. In this work, local crack extensions are allowed to cross grain boundaries. For instance, cracks can propagate from nodes j_1 and j_2 directly to the nodes j_1' and j_2' while crossing a grain boundary. However, the direction of D_5 localization (used to calculate Φ^{crit}) evaluated at crack front nodes j_1 and j_2 could become irrelevant for the portion of the crack spanning from the grain boundary to nodes j_1' and j_2'. While this could impact crack surface crystallography, we believe the impact is minimal given that the crack extensions (~4 μm) are quite small relative to the grain size (~27 μm).

Recognizing that the lack of a strong crack-surface texture occurs in our simulations due to modeling implementations (albeit well-justified and consistent with currently available mechanics insight), it is worth pointing out that experimental observations of crack-surface crystallography using 3D imaging techniques have similarly revealed little to no texture on MSC surfaces for various material systems. For instance, crack growth on classic slip planes (i.e., stage-I) was not observed in Al alloys 7075-T651 and 7050-T7451 in work by Gupta et al. [27] and was rarely observed in an Al–Mg–Si alloy by Spear et al. [20] and in a Ti alloy by Herbig et al. [28]. Therefore, we hypothesize a correlation between the crack-surface crystallography observed in our simulations and the experimental observations; however, establishing a causal relationship between the two would require further investigation.

3.3. Geometric variability of virtually observed crack surfaces

Crack-surface tortuosity (Eq. (10)) is quantified to evaluate geometric variability among the virtually observed crack surfaces for the entire population of 40 microstructures. Fig. 11 shows the distribution of tortuosity at each crack growth step, k. Because cracks are initially flat, the best-fit plane coincides with the respective crack surfaces, at $k = 0$, which leads to a unit tortuosity for all initial cracks. As the crack grows and begins to deflect in response to the microstructure, the best-fit plane no longer coincides with the crack surface, causing an increase in the tortuosity. The crack path in each instantiation was observed to be unique, leading to a right-skewed distribution of tortuosity at each crack growth step. Because the global geometry and loading conditions are identical for all 40 instantiations, we attribute differences observed in tortuosity within a given crack growth increment to microstructural variability in the population. As each crack grows and intersects more grains along the crack front, the right-tail of the distribution gets longer indicating an overall increase in the tortuosity with crack growth. A standard t-test conducted between the distributions corresponding to $k = 1$ and $k = 4$ suggests the existence of a statistically significant difference between the means of the respective distributions. It is worth mentioning that the increase in tortuosity is not caused by a mere increase in area from $k = 1$ to $k = 4$ because tortuosity is a ratio of areas. Therefore, a statistically significant increase in tortuosity should indicate an inherent increase in the frequency of crack path switching with crack growth.

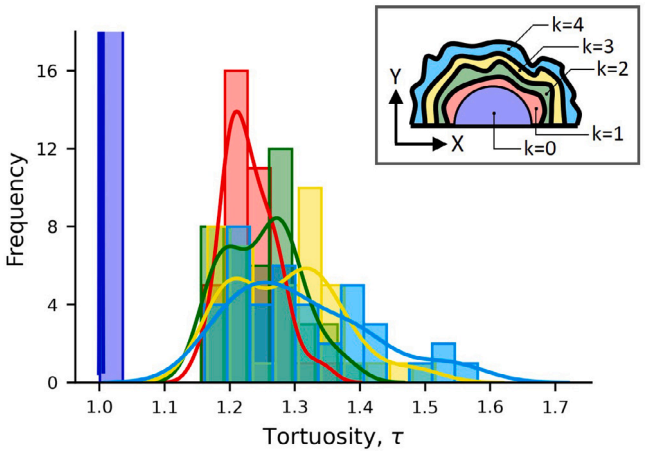

Fig. 11. Tortuosity distribution of simulated MSCs from 40 microstructural instantiations at each crack growth step, k.

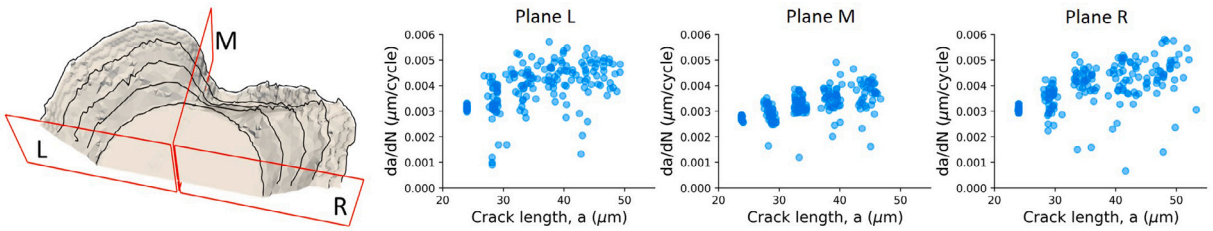

Fig. 12. Crack growth rate plotted as a function of crack length on three distinct planes from all 40 instantiations. The position of the planes is shown for illustration in one of the 40 simulated crack surfaces.

3.4. Variability in MSC growth rate: surface vs. subsurface

Variability in local crack growth rate (evaluated at five crack growth increments in 40 instantiations) plotted as a function of crack length on three distinct planes is shown in Fig. 12. Planes L and R are placed such that they capture the near-free-surface growth of MSCs, which might be observed in a typical experiment. Plane M is placed such that it captures the deep subsurface propagation of the MSCs. The growth rate observed in all three planes exhibits a general increasing trend with the crack length but with significant variability. The mean and standard deviation of growth rate observed on planes L and R combined is 3.85 ± 0.86 nm/cycle, whereas, on plane M, it is 3.2 ± 0.54 nm/cycle. It is noted that the growth rates in our simulations fall under the range of growth rates reported experimentally for comparable crack size in FCC materials [26,29,30]. Because all 40 microstructural instantiations had identical global geometry and boundary conditions, the scatter observed in any given plane is driven by the microstructural aspects. An increase in the mean suggests that the MSCs grow about 20% faster near the free surface compared to the subsurface. A 59% higher standard deviation on planes L and R than on plane M suggests that the presence of free surface can significantly amplify the effects of microstructure on MSCs, in addition to increasing the growth rate.

3.5. Variability in kink angle

The distribution of kink angle, Φ^{crit}, at any particular crack growth step is found to be non-uniform and often bimodal. Therefore, non-parametric box-and-whisker plots that are appropriate for visualizing variations without making assumptions about the underlying distribution have been used in Fig. 13 to show variations in Φ^{crit}. The colored box in Fig. 13 represents the second and third quartiles (aka inter-quartile range) separated by the median line. The lower and upper whiskers are drawn at 1 and 99 percentile, respectively. The extreme one percentile data points are shown as scatter points to alleviate the outliers' influence in the boxplot interpretation. As shown in Fig. 13, Φ^{crit} ranges from $-90°$ to $+90°$ in almost all crack growth steps. The median lines show no apparent trend. However small, there is a consistent increase in the length of the first and fourth quartile, which suggests an increase in the variability of crack deflections with crack growth. This result is consistent with the trend observed in the tortuosity distribution.

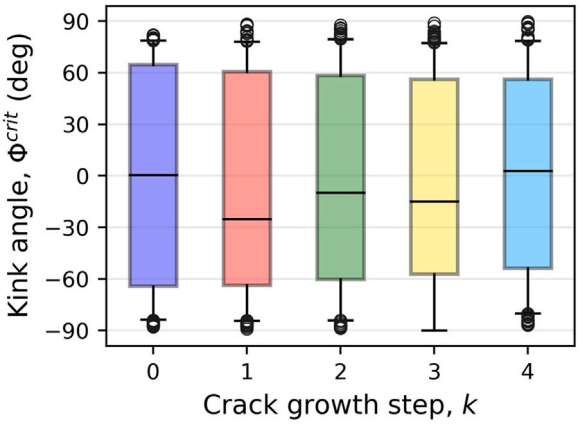

Fig. 13. Boxplot showing the distribution of kink angle calculated at crack front points j as a function of crack growth step, k.

3.6. Statistical correlation analysis

In this section, candidate features that potentially influence MSC growth are identified and classified into geometric/microstructural or micromechanical categories. The classified features are correlated with the MSC growth parameters, viz., Δa and Φ^{crit}. The correlated features are ranked based on the Pearson correlation coefficient with the objective of identifying the most influential features. Note that the correlation values reported in this section are calculated after combining the data extracted from five crack growth increments in all 40 microstructural instantiations.

3.6.1. Correlation of extracted features with crack extension

Fig. 14a shows Pearson correlation of Δa with a variety of geometric/micromechanical features. The features d^x_{fs} and d^y_{fs} represent the shortest distance of the crack front point to the free surface ahead of the crack front in the X and Y-direction, respectively. These features are included to capture the free surface's influence on Δa. The correlation coefficients of d^x_{fs} and d^y_{fs} with Δa implies that the crack front points near the free surface grow relatively faster than those along the rest of the crack front. This is likely due to less material constraint experienced by the crack front points closer to the free surface. The crack length normalized by the average grain diameter, a/d, correlates weakly with Δa. Note that despite the well-established relationship between crack growth rate and crack size in continuum fracture mechanics, MSCs exhibit a very weak correlation. The other candidate microstructural features chosen based on literature, including the average disorientation (ω_{avg}) [31], the average sum of top-five Schmid factors ($\sum_1^5 m$) [32,33], and the tilt ($\Omega_{\lambda_{clos}}$) and twist ($\Psi_{\lambda_{clos}}$) angles of the slip plane relative to the crack orientation [8,34], exhibited a poor correlation with Δa in our study, indicating the limited generalization of these features across the 40 observations.

Correlation coefficients between the local crack extension and a variety of volume-averaged micromechanical field variables calculated ahead of the crack front are shown in Fig. 14b. Among the features investigated, the equivalent plastic strain, ϵ^p_{eq}, and the D_5 metric had the highest correlation with Δa. In a study involving single crystals, Castelluccio et al. [35] found a linear relationship between ΔCTD and a FIP similar to D_5. Our work involving polycrystals reveals a strong relationship between Δa (modeled as a linear function of ΔCTD) and D_5. However, the relationship is not perfectly linear, indicating microstructural influence on FIP values. The correlation between Δa and gradient of D_5 is only slightly less than that between Δa and D_5.

The micromechanical Taylor factor, which is the local crystallographic shear accumulation normalized by the local von Mises strain, is another feature that correlates well with Δa. Raabe et al. [36] introduced the micromechanical Taylor factor to better investigate strain heterogeneity in polycrystals. They also used its gradient to separate in-grain kinematics and grain interaction effects. The correlation of Δa with these factors suggests the key role played by grain-scale effects compared to the macroscopic effects of boundary and loading conditions in modulating Δa. Stress triaxiality, or the ratio of hydrostatic stress to the equivalent (or von Mises) stress, is an important parameter in determining continuum scale damage in ductile materials. Stress triaxiality along the crack front represents local crack constraint [37] and has been found to be inversely related to the crack tip opening displacement for long cracks [38]. A negative correlation of Δa with stress triaxiality suggests the existence of such an inverse relationship even at the microstructurally small regime.

The correlation of individual stress and strain components with Δa ranges from < 0.13 to 0.62. The normal strain and normal stresses correlate more strongly with Δa than do shear strains and shear stresses. The correlation of principal strains or the principal stresses is not as strong, suggesting the high correlations we observed with some of the normal strains/stresses are probably load specific and might change with other loading configurations.

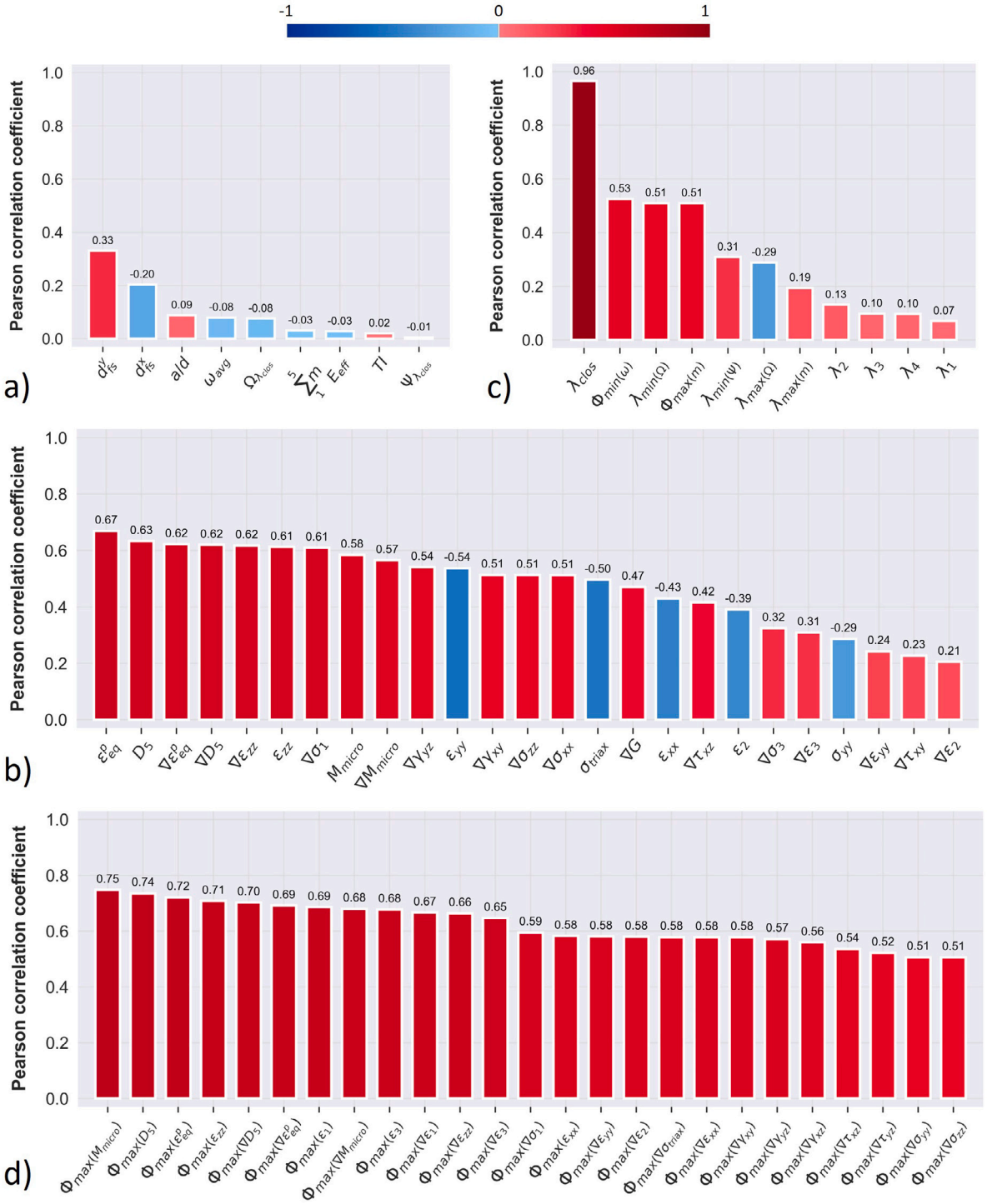

Fig. 14. Pearson correlation coefficients computed between (a) microstructural features and Δa, (b) micromechanical features and Δa, (c) microstructural features and Φ^{crit}, and (d) micromechanical features and Φ^{crit}.

3.6.2. Correlation of extracted features with kink angle

The slip plane angles, i.e., the direction of the intersection of the radial plane with that of the four local slip planes, (111), $(\bar{1}11)$, $(1\bar{1}1)$, and $(\bar{1}\bar{1}1)$ are represented by λ_1, λ_2, λ_3, and λ_4 respectively. It can be seen from Fig. 14c that the kink angle has a very weak correlation with the individual slip plane angles, indicating no preferential crack inclination on a specific slip plane. This is obvious, as we know that different slip planes get activated on different grains along the crack front depending on the local crystal orientation, neighbor orientation, and grain size.

Because the Schmid factor describes the slip systems that can resolve the most shear stress, we investigated its role by correlating $\lambda_{max(m)}$ (the slip plane angle with the maximum total Schmid factor), with kink angle. This feature exhibits a slightly stronger correlation than any specific slip plane angle; however, the relationship is still weak, implying that the role of the Schmid factor is negligible in determining kink angle. To check for the significance of slip plane angles on crack kink, we investigated another feature, λ_{clos}, the closest of the four slip plane angles to the kink angle. This feature lacks any predictive capability, as the kink angle must be known *a priori* to identify the closest slip plane. Nonetheless, a high correlation coefficient emphasizes the fact that the crack deflections indeed occur close to one of the four slip planes.

The other two microstructural features analyzed are $\boldsymbol{\Phi}_{min(\omega)}$, the direction of minimum disorientation between the crystal orientations of crack front point and probe points, and $\boldsymbol{\Phi}_{max(m)}$, which is the direction of the maximum Schmid factor along the probe path. Note for $\boldsymbol{\Phi}_{min(\omega)}$ and $\boldsymbol{\Phi}_{max(m)}$, a unique minima/maxima along the probe could not be found because multiple probe points residing in the same grain yielded a similar value. In cases with such ambiguity, the direction of the probe point closest to the crack's orientation in the previous crack growth step is assigned as the minima/maxima, which is justified based on the energetic standpoint.

The slip plane angle with the minimum tilt, $\lambda_{min(\Omega)}$, shows a positive correlation with the kink angle, while the slip plane angle with the maximum tilt, $\lambda_{max(\Omega)}$, exhibits a negative correlation. This suggests that MSC growth tends to follow a path that minimizes the tilt angle. Additionally, the slip plane angle with the minimum twist angle, $\lambda_{min(\Psi)}$, is positively correlated with the kink angle, although this correlation is weaker compared to that of $\lambda_{min(\Omega)}$.

The strength of the linear relationship between the kink angle and a variety of direction-dependent micromechanical field variables evaluated at each crack front point is presented in Fig. 14d. The correlation of micromechanical Taylor factor, $\boldsymbol{\Phi}_{max(M_{micro})}$ with kink angle has the maximum value of 0.75. Correlation of direction-dependent D_5 metric, $\boldsymbol{\Phi}_{max(D_5)}$, with kink angle has a value of 0.74. This is expected as kink angle itself is derived from the direction of maximum D_5 along the non-local probe. The reason for the lack of unity correlation coefficient is due to the grain conditioning applied after collecting the direction of maximum D_5 metric to determine kink angle. In general, compared to the direction of maximum stress and strain components, the direction in which the gradients of such components are maximized has stronger correlation with kink angle. The direction-dependent stress triaxiality gradient, $\boldsymbol{\Phi}_{max(\nabla\sigma_{triax})}$, is another feature that correlates strongly with kink angle. It is noted that the direction-dependent stress triaxiality, $\boldsymbol{\Phi}_{max(\sigma_{triax})}$, itself, had a very poor correlation with kink angle.

Overall, the correlation study revealed some of the most influential features in controlling MSC growth parameters. However, it can be seen from Sections 3.6.1 and 3.6.2 that a variety of geometric/microstructural and micromechanical features and an interplay between them can influence MSC growth, indicating that the MSC growth phenomenon is indeed complex and requires a holistic approach for the development of predictive models.

3.7. Limitations and implications

There are four limitations that must be acknowledged. First, the simulations treat grain boundaries as discrete changes in the material orientation field; however, grain boundary strengthening effects due to dislocation pile-ups are not included in the constitutive model. Second, while simulating MSC growth in discrete growth increments, the stress and strain fields are not mapped from one mesh to the next with incremental crack growth due to computational expense. Third, the crack growth rules are postulated due to ongoing efforts in the community to validate crack-growth criteria [39]. Finally, only the strength of linear relationships between microstructural and micromechanical features and MSC growth parameters is analyzed (via the Pearson correlation coefficient).

Despite the aforementioned limitations, this work offers valuable insights into the statistical aspects of the variability in 3D MSC growth. The collection and subsequent analysis of a substantially large number of 3D MSC growth observations, as presented in this work, is unprecedented, according to the authors' best knowledge. The reported statistical estimates of the variability have direct implications for engineering design, enabling accurate estimations of remaining useful life for components and facilitating informed decisions regarding safety factors during the design phase. The features identified as being highly influential in determining crack growth represent key couplings between the microstructure and MSC growth behavior and lay the groundwork for developing predictive models for MSC growth behavior. For instance, features extracted from a large number of simulated MSCs can be leveraged to train data-driven machine-learning models for rapid predictions of MSC growth parameters. Moreover, the simulation and analysis techniques used in this work are generic and can be readily extended to estimate the variability in 3D crack growth in other materials.

4. Conclusion

A high-fidelity modeling framework was used to simulate the growth of 3D microstructurally small cracks (MSCs) in 40 instantiations of 3D polycrystals. The crack growth was simulated incrementally, wherein the magnitude and direction of crack growth at each step were informed by the cyclic crack tip displacement range and D_5-fatigue indicator metric, respectively. Data from the 40 simulations were sampled using various data extraction strategies to study the crystallography of the crack surface, quantify the statistical variability of MSC growth, and conduct statistical correlation analysis to find highly influential features governing MSC growth. Based on the results, the following conclusions are drawn:

- Crystallographic analysis of the 40 propagated crack surfaces revealed a lack of preferential crack growth along {111} slip planes despite crack traces on radial planes being closely aligned with {111} slip plane traces. The discrepancy between trace-based observations and 3D surface-based observations is explained by visualizing slip- and crack-plane interactions in 3D.
- The local kink angle of the crack (and the direction of D_5 localization) is mostly influenced by the tilt angle of the grain with respect to the crack plane, while the twist angle has a minor effect.
- The free-surface interaction can significantly accelerate the growth rate of MSCs. Statistically (based on 40 simulated MSCs), portions of the 3D crack front closer to the free surface exhibited a 20% higher mean growth rate, with 59% higher variability compared to those far from the free surface.
- The local crack extension evaluated behind the crack front at each growth step correlated well with many of the candidate micromechanical features extracted ahead of the crack front. Equivalent plastic strain and its gradient, D_5 metric and its gradient, and micromechanical Taylor factor are some of the highly correlated features with crack growth rate. The candidate microstructural features investigated in this work, however, correlated poorly with crack extension.
- The kink angle exhibited a strong correlation with both microstructural and micromechanical features. The most strongly correlated micromechanical features with kink angle are the angles of: maximum micromechanical Taylor factor, maximum equivalent plastic strain, and maximum principal strain. The angle of minimum disorientation, the angle of the slip plane with minimum tilt angle, the angle of maximum Schmid factor, and the angle of the slip plane with minimum twist angle are the most strongly correlated microstructural features.

In conclusion, our work provides new insights into the factors influencing the variability in MSC growth, backed by statistical significance. Collectively, the length scale, detail, dimensionality, and quantity of observations provided here are, to the best of our knowledge, unprecedented for MSCs. These findings have direct implications for engineering design and predictive modeling. In the future, the application of machine learning techniques to analyze large datasets generated in this work can open new avenues for rapid residual life prediction and design optimization in engineering applications.

CRediT authorship contribution statement

Vignesh Babu Rao: Writing – original draft, Visualization, Software, Methodology, Investigation, Formal analysis. **Brian R. Phung:** Software, Methodology. **Bjorn T. Johnsson:** Investigation. **Ashley D. Spear:** Writing – review & editing, Supervision, Resources, Funding acquisition, Conceptualization.

Declaration of competing interest

The authors declare that they have no known competing financial interests or personal relationships that could have appeared to influence the work reported in this paper.

Data availability

We have shared the available data as Supplementary Material.

Acknowledgments

This material is based upon work supported by the National Science Foundation under Grant No. CMMI-1752400. The authors would like to acknowledge the computational resources provided by the University of Utah's Center for High Performance Computing. The authors would like to acknowledge Junyan He and Karen DeMille for the fruitful discussions.

Appendix A

Fig. 15 presents a compilation of all 40 synthetic microstructural instantiations generated using DREAM.3D, each consisting of 150 × 75 × 100 voxels. While each instantiation is unique, they are all derived from the same grain statistics with random crystal orientations, as discussed in Section 2.1.1. Initially, each instantiation is introduced with a flat semi-circular crack, which is subsequently propagated in increments using high-fidelity numerical simulations. The resulting crack surfaces after four propagation steps are visualized in Fig. 16. Note that the 40 crack surfaces in Fig. 16 correspond directly to the 40 microstructures in Fig. 15. The IPF colors on the crack surfaces indicate the local crack-facet normals resolved in the crystal reference frame.

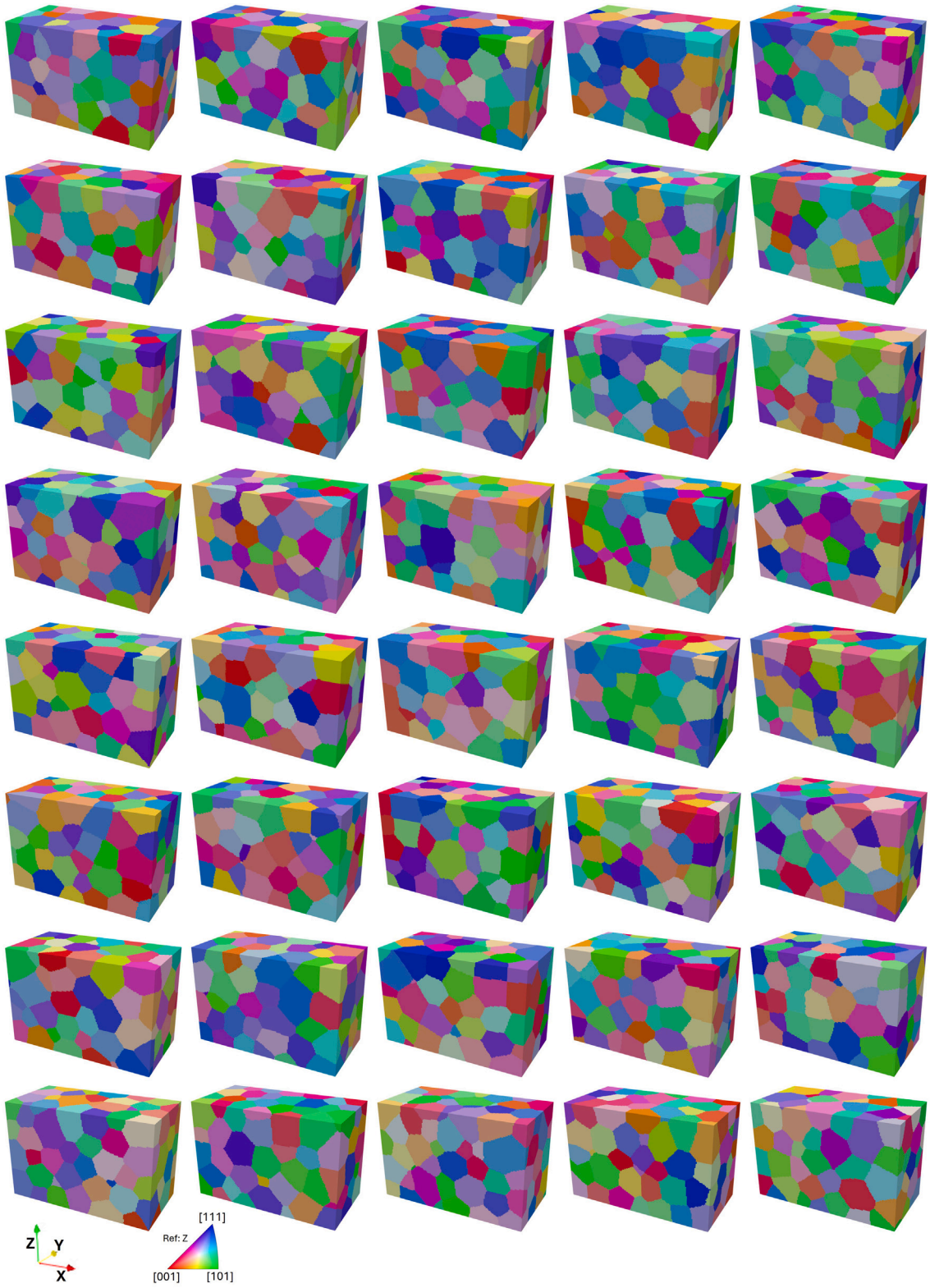

Fig. 15. A collection of all 40 microstructural instantiations used in the MSC growth simulations. The IPF colors represent the crystal orientation of grains in each instantiation.

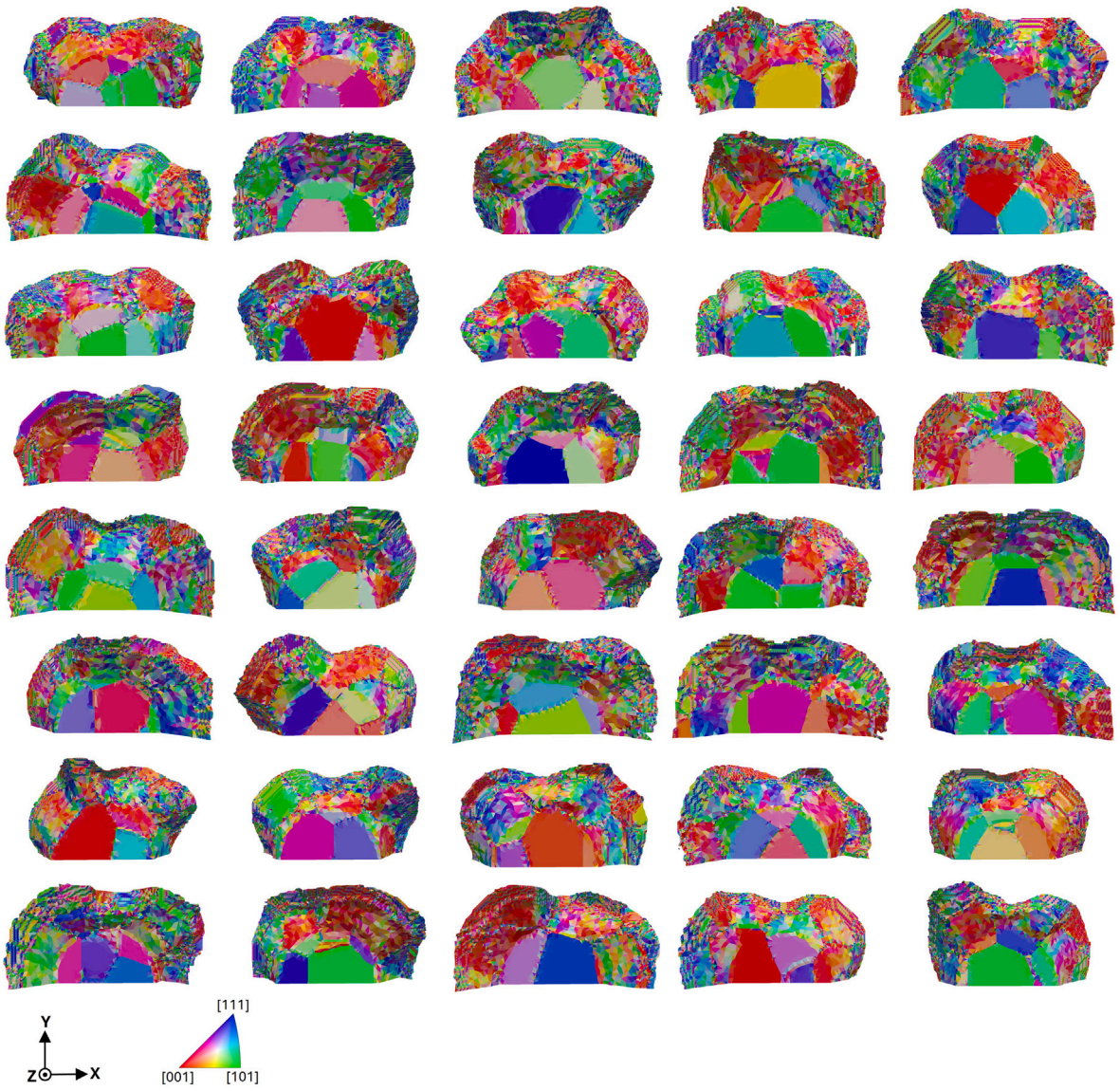

Fig. 16. Crack-surface crystallography of all 40 propagated MSCs obtained from simulations corresponding directly to the microstructures presented in Fig. 15.

Appendix B. Supplementary data

Supplementary material related to this article can be found online at https://doi.org/10.1016/j.engfracmech.2024.110282.

References

[1] Chan KS. Growth characteristics of small fatigue cracks. In: Encyclopedia of tribology. 2013, p. 1592–605. http://dx.doi.org/10.1007/978-0-387-92897-5.
[2] Davidson DL. How fatigue cracks grow, interact with microstructure, and lose similitude. In: ASTM Special technical publication, vol. 1296, 1997, p. 287–300. http://dx.doi.org/10.1520/stp16239s.
[3] Suresh S. Fatigue of materials. second ed.. Cambridge University Press; 1998, p. 224–5. http://dx.doi.org/10.1007/978-0-387-92897-5_100470.
[4] Brockenbrough JR, Hinkle AJ, Magnusen PE, Bucci RJ. Microstructurally based model of fatigue initiation and growth. In: FAA/NASA international symposium on advanced structural integrity methods for airframe durability and damage tolerance, vol. 8, (6):1994, p. 71–84.
[5] Neumann P. Coarse slip model of fatigue. Acta Metall 1969;17(9):1219–25. http://dx.doi.org/10.1016/0001-6160(69)90099-6.
[6] Neumann P. The geometry of slip processes at a propagating fatigue crack-II. Acta Metall 1974;22(9):1167–78. http://dx.doi.org/10.1016/0001-6160(74)90072-8.
[7] Künkler B, Düber O, Köster P, Krupp U, Fritzen CP, Christ HJ. Modelling of short crack propagation - transition from stage I to stage II. Eng Fract Mech 2008;75(3–4):715–25. http://dx.doi.org/10.1016/j.engfracmech.2007.02.018.

[8] Zhai T, Wilkinson AJ, Martin JW. Crystallographic mechanism for fatigue crack propagation through grain boundaries. Acta Mater 2000;48(20):4917–27. http://dx.doi.org/10.1016/S1359-6454(00)00214-7.

[9] McDowell DL, Dunne FP. Microstructure-sensitive computational modeling of fatigue crack formation. Int J Fatigue 2010;32(9):1521–42. http://dx.doi.org/10.1016/j.ijfatigue.2010.01.003.

[10] Rovinelli A, Guilhem Y, Proudhon H, Lebensohn RA, Ludwig W, Sangid MD. Assessing reliability of fatigue indicator parameters for small crack growth via a probabilistic framework. Modelling Simul Mater Sci Eng 2017;25(4). http://dx.doi.org/10.1088/1361-651X/aa6c45.

[11] Rovinelli A, Sangid MD, Proudhon H, Guilhem Y, Lebensohn RA, Ludwig W. Predicting the 3D fatigue crack growth rate of small cracks using multimodal data via Bayesian networks: In-situ experiments and crystal plasticity simulations. J Mech Phys Solids 2018;115:208–29. http://dx.doi.org/10.1016/j.jmps.2018.03.007.

[12] Proudhon H, Li J, Ludwig W, Roos A, Forest S. Simulation of short fatigue crack propagation in a 3D experimental microstructure. Adv Energy Mater 2017;19(8):1–9. http://dx.doi.org/10.1002/adem.201600721.

[13] Hochhalter JD, Littlewood DJ, Christ RJ, Veilleux MG, Bozek JE, Ingraffea AR, et al. A geometric approach to modeling microstructurally small fatigue crack formation: II. Physically based modeling of microstructure-dependent slip localization and actuation of the crack nucleation mechanism in AA 7075-T651. Modelling Simul Mater Sci Eng 2010;18(4):045004. http://dx.doi.org/10.1088/0965-0393/18/4/045004.

[14] Phung BR, Spear AD. A voxel-based remeshing framework for the simulation of arbitrary three-dimensional crack growth in heterogeneous materials. Eng Fract Mech 2019;209:404–22. http://dx.doi.org/10.1016/j.engfracmech.2019.01.008.

[15] Phung BR, He J, Spear AD. A surface-mesh gradation tool for generating gradated tetrahedral meshes of microstructures with defects. Comput Mater Sci 2021;197:110622. http://dx.doi.org/10.1016/j.commatsci.2021.110622.

[16] Groeber MA, Jackson MA. Dream.3D: A digital representation environment for the analysis of microstructure in 3D. Integr Mater Manuf Innov 2014;3(1):56–72. http://dx.doi.org/10.1186/2193-9772-3-5.

[17] Spear AD, Ingraffea AR. Effect of chemical milling on low-cycle fatigue behavior of an Al-Mg-Si alloy. Corros Sci 2013;68:144–53. http://dx.doi.org/10.1016/j.corsci.2012.11.006.

[18] Stopka KS, Yaghoobi M, Allison JE, McDowell DL. Effects of boundary conditions on microstructure-sensitive fatigue crystal plasticity analysis. Integr Mater Manuf Innov 2021;10(3):393–412. http://dx.doi.org/10.1007/s40192-021-00219-2.

[19] Matouš K, Maniatty AM. Finite element formulation for modelling large deformations in elasto-viscoplastic polycrystals. Internat J Numer Methods Engrg 2004;60(14):2313–33. http://dx.doi.org/10.1002/nme.1045.

[20] Spear AD. Numerical and experimental studies of three-dimensional crack evolution in aluminum alloys: macroscale to microscale (Ph.D. thesis), (May). Cornell University; 2014.

[21] McDowell DL, Gall K, Horstemeyer MF, Fan J. Microstructure-based fatigue modeling of cast A356-T6 alloy. Eng Fract Mech 2003;70(1):49–80. http://dx.doi.org/10.1016/S0013-7944(02)00021-8.

[22] Castelluccio GM, McDowell DL. Mesoscale modeling of microstructurally small fatigue cracks in metallic polycrystals. Mater Sci Eng A 2014;598:34–55. http://dx.doi.org/10.1016/j.msea.2014.01.015.

[23] Shyam A, Lara-Curzio E. A model for the formation of fatigue striations and its relationship with small fatigue crack growth in an aluminum alloy. Int J Fatigue 2010;32(11):1843–52. http://dx.doi.org/10.1016/j.ijfatigue.2010.05.005.

[24] Lankford J, Davidson DL, Chan KS. The influence of crack tip plasticity in the growth of small fatigue cracks. Metall Trans A 1984;15(8):1579–88. http://dx.doi.org/10.1007/BF02657797.

[25] Johnstone DN, Martineau BH, Crout P, Midgley PA, Eggeman AS. Density-based clustering of crystal (mis)orientations and the orix python library. J Appl Crystallogr 2020;53:1293–8. http://dx.doi.org/10.1107/S1600576720011103.

[26] Menasche DB, Shade PA, Kenesei P, Park JS, Musinski WD. Four-dimensional microstructurally small fatigue crack growth in cyclically loaded nickel superalloy specimen. Int J Fatigue 2023;177:107920. http://dx.doi.org/10.1016/j.ijfatigue.2023.107920.

[27] Gupta VK, Agnew SR. Fatigue crack surface crystallography near crack initiating particle clusters in precipitation hardened legacy and modern Al-Zn-Mg-Cu alloys. Int J Fatigue 2011;33(9):1159–74. http://dx.doi.org/10.1016/j.ijfatigue.2011.01.018.

[28] Herbig M, King A, Reischig P, Proudhon H, Lauridsen EM, Marrow J, et al. 3-D growth of a short fatigue crack within a polycrystalline microstructure studied using combined diffraction and phase-contrast X-ray tomography. Acta Mater 2011;59(2):590–601. http://dx.doi.org/10.1016/j.actamat.2010.09.063.

[29] Spear AD, Li SF, Lind JF, Suter RM, Ingraffea AR. Three-dimensional characterization of microstructurally small fatigue-crack evolution using quantitative fractography combined with post-mortem X-ray tomography and high-energy X-ray diffraction microscopy. Acta Mater 2014;76:413–24. http://dx.doi.org/10.1016/j.actamat.2014.05.021.

[30] Li J, Huang Q, Wang Z, Zhang N, Chen G, Qian G. Microstructural insights into fatigue short crack propagation resistance and rate fluctuation in a Ni-based superalloy manufactured by laser powder bed fusion. Int J Plast 2023;171:103800. http://dx.doi.org/10.1016/j.ijplas.2023.103800.

[31] Peralta P, Dickerson R, Dellan N, Komandur K, Jameel MA. Effects of local grain orientation on fatigue crack growth in multicrystalline fcc metallic materials. J Eng Mater Technol 2005;127(1):23–32. http://dx.doi.org/10.1115/1.1836768.

[32] Motoyashiki Y, Brückner-Foit A, Sugeta A. Microstructural influence on small fatigue cracks in a ferritic-martensitic steel. Eng Fract Mech 2008;75(3–4):768–78. http://dx.doi.org/10.1016/j.engfracmech.2007.04.019.

[33] Hassanipour M, Watanabe S, Hirayama K, Toda H, Uesugi K, Takeuchi A. Short crack growth behavior and its transitional interaction with 3D microstructure in Ti-6Al-4V. Mater Sci Eng A 2018;738:229–37. http://dx.doi.org/10.1016/j.msea.2018.09.073.

[34] Ludwig W, Buffière JY, Savelli S, Cloetens P. Study of the interaction of a short fatigue crack with grain boundaries in a cast Al alloy using X-ray microtomography. Acta Mater 2003;51(3):585–98. http://dx.doi.org/10.1016/S1359-6454(02)00320-8.

[35] Castelluccio GM, McDowell DL. Assessment of small fatigue crack growth driving forces in single crystals with and without slip bands. Int J Fract 2012;176(1):49–64. http://dx.doi.org/10.1007/s10704-012-9726-y.

[36] Raabe D, Sachtleber M, Zhao Z, Roters F, Zaefferer S. Micromechanical and macromechanical effects in grain scale polycrystal plasticity experimentation and simulation. Acta Mater 2001;49(17):3433–41. http://dx.doi.org/10.1016/S1359-6454(01)00242-7.

[37] Brocks W, Künecke G. On the influence of triaxiality of the stress state on ductile tearing resistance. In: Defect assessment in components - fundamentals and applications. London: Mechanical Engineering Publications; 1991, p. 189–201.

[38] Wang TJ, Li DJ, Ma FS, Kuang ZB. Influence of stress triaxiality on damage and crack tip opening displacement parameters for steels. Theor Appl Fract Mech 1995;22(2):151–8. http://dx.doi.org/10.1016/0167-8442(94)00055-6.

[39] Phung B, Greeley DA, Yaghoobi M, Adams JF, Allison J, Spear A. Predicting microstructurally sensitive fatigue-crack path in WE43 magnesium using high-fidelity numerical modeling and three-dimensional experimental characterization. Fatigue Fract Eng Mater Struct 2024;47(3):862–83. http://dx.doi.org/10.1111/ffe.14210.